nature communications

Article

https://doi.org/10.1038/s41467-026-77636-4

Multi-interface electrical double layers dynamics as a unified platform for power generation and environmental intelligence

Received: 16 November 2025

Accepted: 28 August 2026

Published online: 09 September 2026

Check for updates

Youbo Nan[1,2,3], Xiang Li[2,3], Xiutong Wang[1] ✉, Yan Du[2], Jiaxin Hu[2], Rongbing Han[2], Baodong Chen[2] ✉, Zhong Lin Wang[2] ✉ & Di Wei[2] ✉

Electrical double layers (EDLs) at solid-liquid interfaces mediate charge separation and ion transport, but their dynamic use for both energy harvesting and sensing in open water remains limited. Here we show that wave-driven multi-interface electrical double layers in a tubular dielectric architecture can couple power generation with environmental perception. Periodic water motion assembles and disrupts coupled inner and outer interfacial layers, producing a charge-relay and parallel-release process that enhances charge transfer and short-circuit current to levels sufficient for low-power sensing. The same ion motion that generates electricity also encodes hydrodynamic and spatial perturbations as current signatures. Inspired by weakly electric fish, we organize these signatures using a main-auxiliary electrode network that amplifies directional responses and enables coating monitoring, wave-state recognition and two-dimensional localization. This work establishes dynamic multi-interface electrical double layers as a physical platform for self-powered hydrospheric sensing and spatially resolved environmental perception.

The hydrospheric interface, covering oceans, lakes, and their near-surface regions, is a central arena of energy exchange, material transport, and human activity[1–4]. Deploying intelligent systems that operate at this dynamic interface to monitor environments, forecast ecology, protect against corrosion, and resolve spatial information is essential for hydrospheric interface exploration, safety, and sustainability. However, most current systems still rely on fossil-fuel-powered electromagnetic generation, with unsustainable supply, costly maintenance, and ecological costs[5–7]. Meanwhile, existing sensing and localization technologies, including acoustic detection, radar, automatic identification systems (AIS), and optical remote sensing, remain intrinsically reliant on external power supplies or onboard batteries to generate active emissions or detect specific target signatures. Such dependence not only limits operational endurance but also exposes these systems to severe signal attenuation, multipath interference, and environmental noise, particularly in complex aquatic environments[8–11]. Their active nature further renders them vulnerable to signal spoofing and distortion, resulting in significant degradation of detection reliability. In addition, power supply, sensing, and communication functions are typically implemented as discrete modules, creating inefficiencies that hinder system miniaturization, long-term autonomy, and scalable network deployment. These challenges underscore the urgent need for an integrated physical framework in which power generation and adaptive signal perception are intrinsically coupled, enabling self-sustained and intelligent hydrospheric monitoring.

The electrical double layers (EDLs), ubiquitous at liquid–solid interfaces, provide such a platform[12]. As a fundamental interfacial unit, the EDLs govern charge separation, migration, and reconstruction at

[1]State Key Laboratory of Advanced Marine Materials and Shandong Key Laboratory of Marine Environmental Corrosion and Bio-fouling, Institute of Oceanology, Chinese Academy of Sciences, Qingdao, China. [2]Beijing Institute of Nanoenergy and Nanosystems, Chinese Academy of Sciences, Beijing, China. [3]These authors contributed equally: Youbo Nan, Xiang Li. ✉e-mail: wangxiutong@qdio.ac.cn; chenbaodong@binn.cas.cn; zlwang@binn.cas.cn; weidi@binn.cas.cn

the nanoscale and have long played a vital role in electrochemical systems such as electrocatalysis, batteries, and supercapacitors[13–15]. Recently, a two-step model for EDLs at insulating dielectric-liquid interfaces has been proposed, in which ions and electrons jointly build a tightly ionic-electronic coupling interface[16,17]. Dynamic regulation of this interface enables efficient ionic-electronic coupling transfer in devices. Ionotronics transcends conventional electronics, enabling multivalent ions to act as tunable carriers for coupled charge transport and information modulation, offering great potential in energy conversion and sensing[18–23]. This mechanism has been demonstrated in diverse applications, including raindrop energy generators, wave-driven nanogenerators, self-powered human-machine interfaces, and interfacial probes[24–26]. However, these studies have been predominantly validated in localized, near-field configurations (centimeter-scale), most often based on straight-electrode-driven contact-separation geometries or droplet-scale interfacial manipulation[27–30]. Directly harnessing wave motion in aquatic environments to couple energy harvesting with spatially decodable sensing remains far less explored. Critically, the EDLs establish a natural physical link between energy flow and information flow, as the very process of energy transfer encodes the environmental signal. With appropriate control of charge redistribution in the Stern layer, ion migration in the diffuse layer, and transport within the Debye length, EDLs can implement signal encoding and transmission, enabling underwater communication, ionic neuromorphic circuits, and logic operations[29,31,32]. Despite this prospect, high-precision spatial localization and directional resolution in complex aquatic environments remain challenging due to attenuation and multi-dimensional coupling.

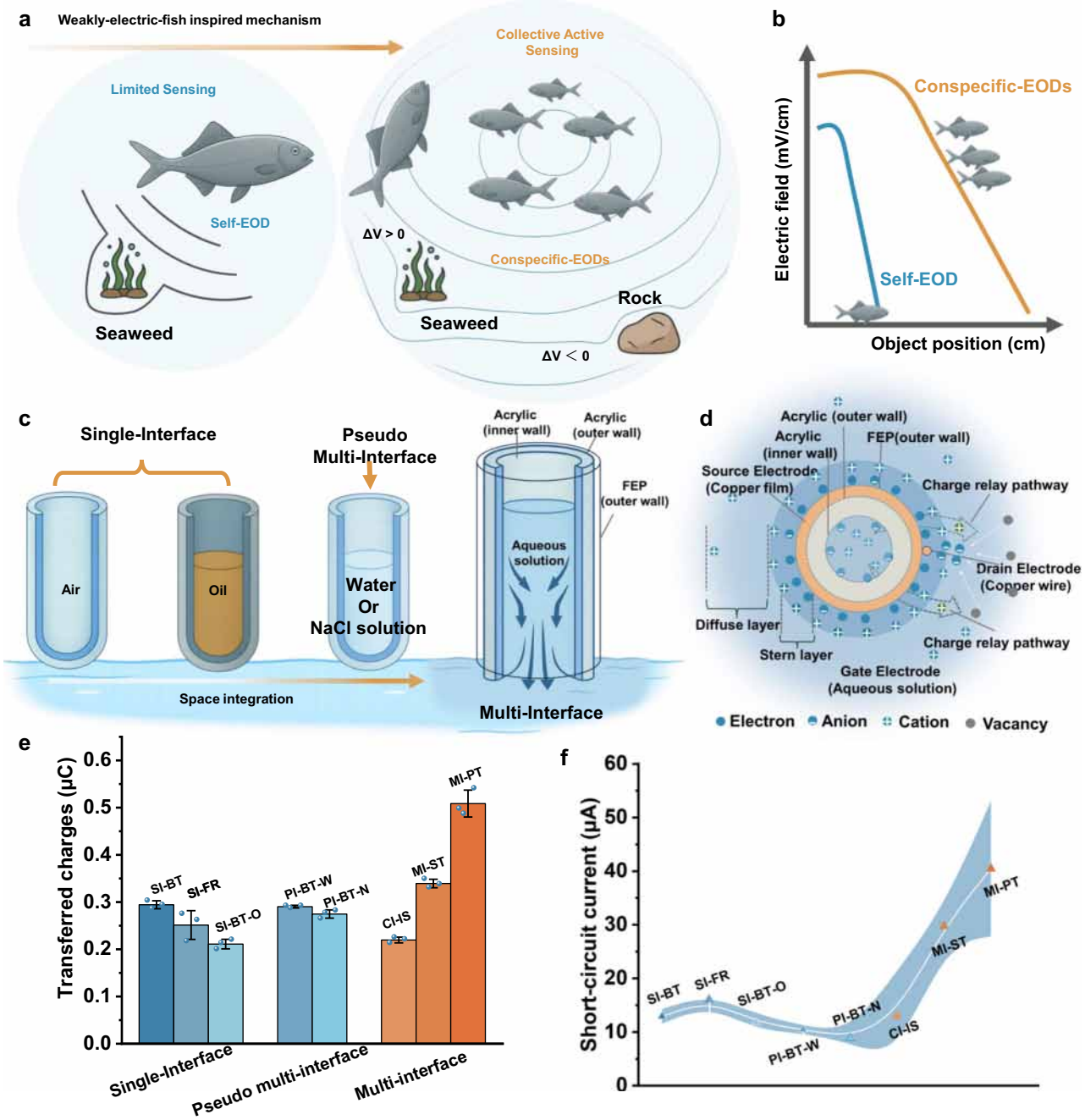
In nature, weakly electric fish (widely distributed in South America and Africa, e.g., Gnathonemus petersii) have evolved a remarkably efficient electrosensory system that operates at low power while achieving high spatial resolution, enabling precise environmental perception and navigation in complex aquatic habitats[33,34]. Unlike strongly electric fish that hunt via high-voltage discharges[35], weakly electric fish periodically emit millivolt-level electric organ discharges (EODs), forming a stable three-dimensional field for environmental probing and active electrolocation[36–38]. Specifically, cutaneous electroreceptor arrays, together with the electrosensory lateral line lobe, transduce perturbations in the self-generated electric field into a spatiotemporal contrast code characterized by a signed amplitude (ΔV), where conductive objects locally enhance the field and insulators attenuate it. The polarity of ΔV indicates whether field lines converge or diverge, thereby providing material information, while its magnitude correlates with target distance, size, and electrical contrast, enabling centimeter-scale electrolocation. Nevertheless, the effective sensing range of an individual fish is inherently limited by the rapid spatial decay of its self-generated EODs, particularly when encountering weakly reflective or distant objects (Fig. 1a, left). For example, nearby seaweed can be readily detected owing to pronounced field perturbations, whereas distant objects such as rocks often lie beyond the perceptual range. Remarkably, when weakly electric fish operate collectively, they employ a cooperative sensing strategy in which the phase and timing of individual discharges are synchronized. Rather than interfering destructively, these coordinated EODs constructively reinforce one another, producing spatially coherent field amplification. This cooperative mechanism extends both the local field strength and the effective sensing radius (Fig. 1a, right), allowing each fish to perceive environmental cues not only from its own EODs but also from those of neighboring conspecifics. Such collective electrolocation, integrating self- and conspecific-derived signals, achieves simultaneous energy transmission and information acquisition within a unified physical process, characterized by exceptional sensitivity and minimal energy consumption (Fig. 1b).

Inspired by this bioelectrical paradigm, we propose a dynamic multi-interface EDL system that achieves the coordinated optimization of power generation and information transmission within a unified physical framework. Here, dynamic multi-interface EDLs are developed beyond localized unit-level responses into a cooperatively decodable sensing architecture for open hydrospheric environments. The device features an acrylic through-tube architecture that forms two coupled interfaces: an outer fluorinated ethylene propylene-water (FEP-water) interface and an inner polymethyl methacrylate-water (PMMA-water) interface. Coupling between these interfaces enables wave-induced disturbances to periodically form and disassemble interfacial EDLs, triggering charge-relay and parallel-release processes that substantially enhance charge transfer (Q_{tr} ≈0.51 μC) and short-circuit current (I_{sc} ≈40.5 μA), nearly doubling the performance of single-interface configurations. This multi-interface cooperative mechanism enables spatially synchronized response enhancement and efficient energy conversion, delivering sufficient output to power low-energy sensors. More importantly, the time-dependent charge redistribution within the dynamic EDLs functions as a decodable information carrier. Following the contrast-coding logic of weakly electric fish, the sign and magnitude of the EDLs response are used to encode local perturbations as spatially interpretable electrical signatures, enabling predictive monitoring of coating integrity as well as real-time classification and warning of wave conditions. Building upon this foundation, and further drawing inspiration from the cooperative sensing behavior of electric fish schools, a main-auxiliary drain network was devised to form an artificial bioinspired electrosensory system capable of directional signal amplification and two-dimensional spatial decoding in open hydrospheric interfaces. Unlike conventional electrode arrays that generally rely on externally powered excitation and distributed sensing, the present architecture is based on iontronic signatures arising from the dynamic multi-interface EDLs system itself, thereby coupling energy generation, signal formation, and spatial sensing within the same physical process. This design offers a physical foundation and engineering strategy for self-powered, distributed, and adaptive intelligent hydrospheric systems.

Results

Cooperative charge-relay enhancement in dynamic multi-interface EDLs systems

The dynamic EDLs at the liquid–solid interface governs nanoscale ion-electron interactions, including charge separation, transfer and reconstruction. As a responsive physical platform for energy conversion, the EDLs can directly transduce environmental disturbances into measurable electrical signals. Based on this principle, dynamic multi-interface EDLs systems have been designed to realize synchronous activation and cooperative enhancement of energy conversion through structural coupling among multiple liquid–solid interfaces. Accordingly, these systems were designed to distinguish geometric interfacial multiplication from connectivity-dependent interfacial coupling. To systematically investigate the effect of interfacial structure on energy-harvesting behavior, three representative EDLs configurations were constructed as illustrated in Fig. 1c: the single-interface blind-tube system (SI-BT), the pseudo-interface blind-tube system (PI-BT), and the multi-interface system (MI). The SI-BT contains only a single active FEP-water interface. The PI-BT structures were prepared by filling the blind tube with either deionized water (PI-BT-W) or 3.5 wt% NaCl solution (PI-BT-N), producing geometrically dual interfaces in which the inner and outer liquid layers remain isolated, preventing interfacial charge coupling. The MI configuration employs an acrylic through-tube with connected-inner and outer liquid channels at the bottom, enabling dynamic interfacial coupling. Collectively, these systems represent a continuum from a single active interface to a geometrically dual but uncoupled design, and finally to a fully coupled multi-interface structure, underscoring the critical role of interfacial connectivity in governing coupling dynamics and enhancing energy conversion efficiency.



In the SI-BT system, a FEP film serves as the dielectric layer coating the outer wall of the acrylic tube. The surrounding aqueous solution acts as the gate electrolyte, while a copper foil source electrode and a copper wire drain electrode facilitate charge induction and collection (Supplementary Figs. 1 and 2). When the liquid is driven by wave-induced reciprocating motion, it periodically contacts and separates from the FEP surface, dynamically forming and disrupting the EDLs and inducing charge accumulation on the interfaces. As the liquid level rises and reaches the drain electrode, charge transfer from the source to the drain is triggered. The detailed working mechanism is illustrated in Supplementary Fig. 3. This process can be equivalently modeled as a series circuit consisting of three capacitors, namely, the FEP dielectric capacitor (C_F), the water/FEP interface capacitor ($C_{W/F}$), and the water/drain interface capacitor ($C_{W/D}$), along with a resistor (R_w) representing the resistance of the electrolyte. It should be noted that the $C_{W/D}$ capacitance forms instantaneously upon contact between the gate solution and the drain electrode. Before this contact occurs, $C_{W/D}$ is ineffective, as shown in Supplementary Fig. 4. The theoretical output peak current (I) can be approximately expressed as:

$$I = \frac{U}{R} = \frac{\sigma_e \Delta S d_F}{(R_w + R_L)\varepsilon_F S_F} = \frac{\sigma_e (S_t - S_0) d_F}{(R_w + R_L)\varepsilon_F S_F} \quad (1)$$

Here, σ_e is the effective surface charge density on the FEP film, and (S_t - S_0) denotes the change in the effective interfacial area (ΔS) induced by the contact between the gate liquid and the drain electrode. d_F is the thickness of the FEP layer, R_w and R_L are the resistances of the electrolyte and external load, respectively, and ε_F and S_F are the dielectric constant and effective charged area of the FEP layer. (For a detailed derivation, refer to Supplementary Note 1)[39]. Because only one electroactive interface participates in the process, the responsive area of the system is limited, resulting in relatively low output performance.

Fig. 1 | Multi-interface electrical double layers (EDLs) charge-relay architecture and performance validation. a Schematic comparison of active electrolocation by an individual weakly electric fish and cooperative electrolocation by a fish school. An individual weakly electric fish emits millivolt-level electric organ discharges (EODs) to form a local electric field for environmental probing. Conductive or insulating objects perturb this field and generate a signed potential contrast (ΔV), but the effective sensing range is limited by rapid field decay. In a fish school, synchronized EODs from neighboring fish reinforce the local electric field, extending the sensing radius and enabling cooperative perception of environmental cues. **b** Comparison of electric sensing signals and perception ranges between an individual weakly electric fish and a fish school. Individual electrolocation produces a localized response, whereas collective electrolocation amplifies field perturbations through coordinated EODs, allowing environmental information to be acquired over a larger spatial range. **c** Schematic comparison of single-interface, pseudo multi-interface and multi-interface electrical double layer (EDL) configurations. The single-interface systems include a single-interface blind-tube system with air inside the tube (SI-BT), and an oil-filled single-interface blind-tube system (SI-BT-O). The pseudo multi-interface systems contain water or NaCl solution inside a blind tube, forming geometrically dual but hydraulically isolated interfaces, denoted as PI-BT-W and PI-BT-N, respectively. The multi-interface system uses an acrylic through-tube to connect the inner and outer aqueous pathways, enabling coupled activation of the inner and outer interfaces. The orange arrow in c indicates the spatial integration from single-interface and pseudo multi-interface configurations to the connected multi-interface architecture. **d** Schematic of the charge-relay process in the multi-interface system. Wave-induced liquid motion dynamically assembles and disrupts EDLs at the outer FEP-water interface and the inner acrylic-water interface. The connected aqueous pathway enables charge redistribution between the coupled interfaces and synchronized charge release through the drain electrode. Electron, anion, cation and vacancy symbols are defined in the schematic. **e** Transferred charge (Q_{tr}) of different device configurations, including single-interface blind-tube system (SI-BT), single-interface FEP rod (SI-FR), oil-filled single-interface blind-tube system (SI-BT-O), pseudo multi-interface blind-tube systems filled with water (PI-BT-W) or NaCl solution (PI-BT-N), connected-inner-wall inactive-state structure (CI-IS), serial-type multi-interface system (MI-ST) and parallel-type multi-interface system (MI-PT). **f** Short-circuit current (I_{sc}) of the corresponding device configurations. In **e**, bars show mean values, dots indicate individual measurements, and error bars represent s.d. from three parallel measurements ($n = 3$). In **f**, lines show mean values and shaded regions represent s.d. from three parallel measurements ($n = 3$).

The SI-BT system produced a Q_{tr} of only 0.29 μC and an I_{sc} of 12.9 μA, as shown in Fig. 1e, f. The corresponding waveform profiles are provided in Supplementary Fig. 5.

To verify that the performance limitation stems from the restricted number of electroactive interfaces, two single-interface control structures were designed for comparison. The single-interface FEP rod (SI-FR) contains only the outer FEP-water interface without any internal surface participation (Supplementary Figs. 6 and 7). The oil-filled blind tube (SI-BT-O) has two geometric interfaces, yet the insulating oil phase prevents the formation of an effective EDL (Supplementary Figs. 8 and 9). Both configurations showed Q_{tr} and I_{sc} values similar to those of the SI-BT, as shown in Fig. 1e, f and Supplementary Fig. 5, indicating that geometric expansion or the presence of electrochemically inert interfaces alone cannot effectively enhance power generation. To further distinguish between geometric dual interfaces and electroactive coupling effects, pseudo-interface systems (PI-BT-W and PI-BT-N) were developed (Supplementary Figs. 10–13). These structures were obtained by filling the blind tube with deionized water or NaCl solution to form dual inner and outer interfaces that remain hydraulically isolated. Because the inner liquid is static and the inner wall does not participate in dynamic EDL formation, the output remains limited. The PI-BT-W structure produces $Q_{tr} = 0.29$ μC and $I_{sc} = 10.5$ μA, while the PI-BT-N structure yields $Q_{tr} = 0.27$ μC and $I_{sc} = 8.9$ μA (Fig. 1e, f and Supplementary Fig. 14). These results indicate that neither an increase in geometric interface number nor the mere presence of an additional inactive interface is sufficient to enhance energy output.

To address the constraints of the single-interface system, a multi-interface (MI) configuration was implemented, establishing liquid connectivity that allows synchronous activation and dynamic charge coupling between the inner and outer interfaces. This configuration markedly enhances charge transport along the liquid pathways, enabling wave-induced perturbations to activate not only the outer-wall EDL but also to propagate through the connected liquid to the inner cavity. Consequently, ions at the inner-wall interface undergo coordinated displacement, generating a cooperative interfacial discharge. In this system, the hydrophobic FEP film on the outer wall (Supplementary Fig. 15a) supports an EDL primarily driven by electron migration, whereas the hydrophilic PMMA inner wall (Supplementary Fig. 15b) establishes an EDL dominated by ion migration[17]. The two interfaces operate within a shared liquid environment, forming a synergistic unit with enhanced charge storage capacity. During wave-induced oscillations, the EDLs at both interfaces are cyclically established and disrupted, generating temporally offset yet spatially coupled discharge pathways. The inner liquid functions as a dynamic charge reservoir, collectively activated under mechanical excitation, which promotes charge redistribution in the outer electrolyte and synchronized ion migration across the interfacial regions. The spatial configuration and charge-relay mechanism of the through-tube system are depicted in Fig. 1d.

Depending on the arrangement and connection of the drain electrodes, the multi-interface system can be classified into a serial-type (MI-ST) and a parallel type (MI-PT). In the MI-ST, a single drain electrode is used, and the oscillating liquid sequentially activates the outer and inner interfaces, forming a serial discharge channel (Supplementary Figs. 16 and 17). In the MI-PT, two drain electrodes are installed and electrically connected, allowing simultaneous charge release from both interfaces and realizing a parallel-type spatial amplification mechanism (Supplementary Figs. 18–20). The results show that the MI-ST achieves $Q_{tr} = 0.34$ μC and $I_{sc} = 29.8$ μA, while the MI-PT further increases these values to $Q_{tr} = 0.51$ μC and $I_{sc} = 40.5$ μA (Fig. 1e, f and Supplementary Fig. 21).

Geometrically, the through-tube design increases the total electroactive interfacial area, with the theoretical surface gain given by

$$\frac{S_{through}}{S_{blind}} = 1 + \frac{D_i}{D_o} \approx 1.88 \quad (2)$$

corresponding to an 88% increase in area (see Supplementary Note 2 for the derivation). This geometric gain provides a plausible structural contribution to the improved output of the MI system, but it is not sufficient to account for the enhancement on its own. To separate the effect of geometric enlargement from that of interfacial coupling, two stringent controls were examined. The connected-inner-wall inactive-state structure (CI-IS) (Supplementary Fig. 22), which preserves the through-tube geometry while suppressing inner-wall activation, yielded only $Q_{tr} = 0.22$ μC and $I_{sc} = 13.5$ μA (Fig. 1e, f and Supplementary Fig. 23). Likewise, an equal-area single-interface planar control (EA-SI), matched to the effective single-interface area of the MI system (Supplementary Fig. 24), showed similarly limited output, with $Q_{tr} = 0.26$ μC and $I_{sc} = 15.1$ μA (Supplementary Fig. 25). Thus, neither matched geometry nor matched area reproduces the response of the MI configuration. Computational fluid dynamics (CFD) simulations further show that fluid perturbations at the outer wall of the through-tube and blind-tube configurations are nearly identical (Supplementary Fig. 26 and Supplementary Movie 1), excluding differences in external hydrodynamic disturbance as the dominant source of the enhancement. Taken together, these controls indicate that the superior output of the MI system arises primarily from liquid-

https://doi.org/10.1038/s41467-026-77636-4

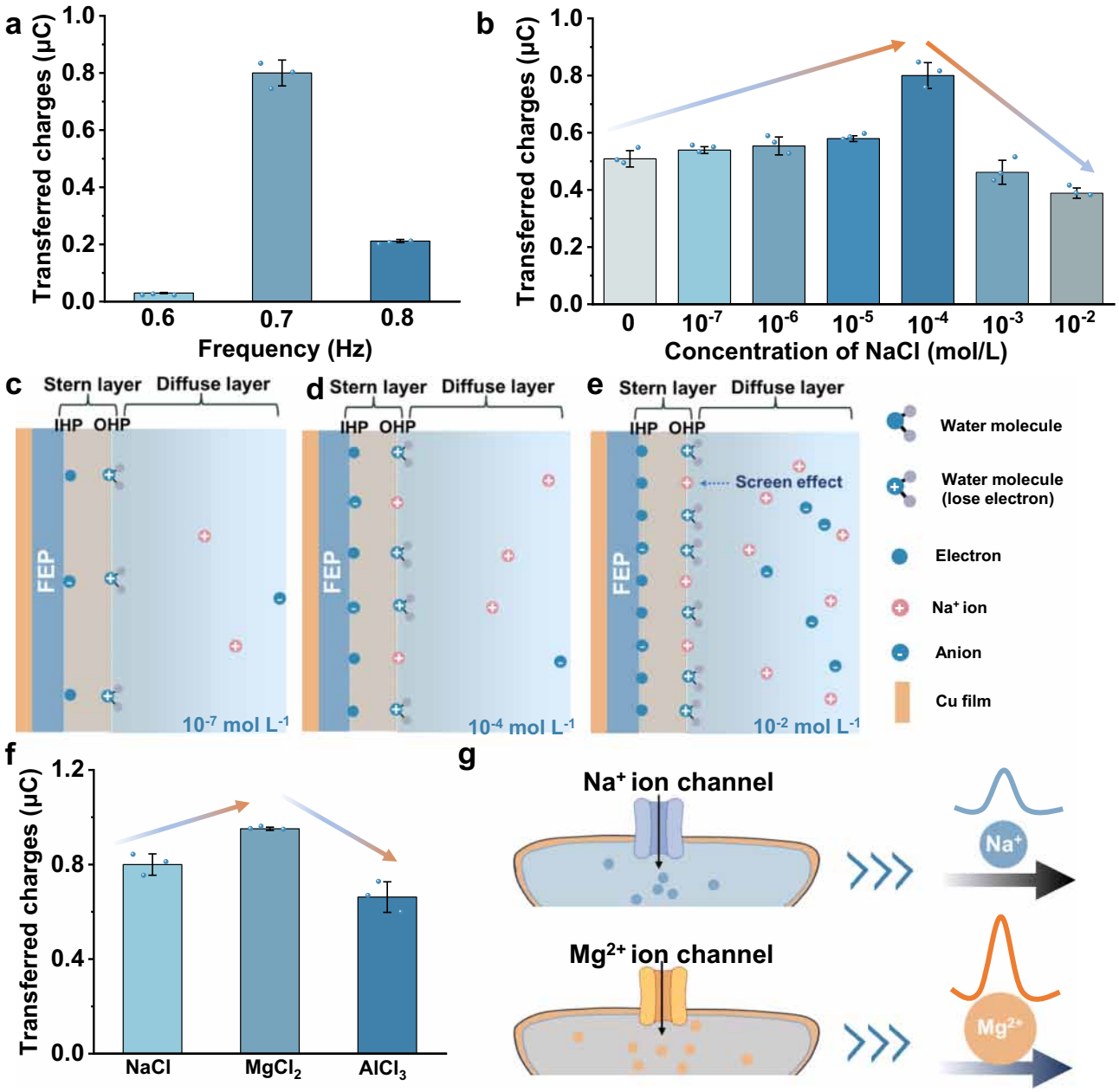


Fig. 2 | Frequency-modulated charge transfer and ionic regulation in multi-interface dynamic EDLs. a Transferred charge (Q_{tr}) of dynamic EDLs with different wave-induced frequencies. **b** Transferred charge (Q_{tr}) versus NaCl concentration from 0 to 10^{-2} mol L^{-1}, showing a non-monotonic optimum at 10^{-4} mol L^{-1}. The arrows indicate the concentration-dependent increase and decrease in Q_{tr}. **c** Schematic diagram of the EDLs structure in low concentration NaCl solution (10^{-7} mol L^{-1}). **d** Schematic diagram of the EDLs structure in medium-concentration NaCl solution (10^{-4} mol L^{-1}). **e** Schematic diagram of the EDLs structure in high-concentration NaCl solution (10^{-2} mol L^{-1}). The schematics show the FEP surface, Cu film, Stern layer, diffuse layer, inner Helmholtz plane (IHP), outer Helmholtz plane (OHP), water molecules, water molecules after electron loss, electrons, Na^+ ions and anions. **f** Cation-specific effects on transferred charge (Q_{tr}) at a constant concentration of 10^{-4} mol L^{-1}. The arrows indicate the ion-specific trend in Q_{tr}. **g** Iontronic framework mirroring energy-information flow in biological systems. The arrows indicate ion transport and signal conversion. In **a**, **b**, **f**, bars show mean values, dots indicate individual measurements and error bars represent s.d. from three parallel measurements ($n = 3$).

connectivity-enabled dynamic coupling and spatiotemporally coordinated charge release between the inner and outer interfaces. Therefore, the wave-driven dynamic multi-interface EDL system achieves synchronous activation and cooperative discharge through liquid connectivity, substantially improving charge participation and energy-conversion efficiency. These results demonstrate the spatial charge-relay enhancement effect in dynamic multi-interface EDL systems and establish a physical basis for efficient power generation and self-powered operation at liquid–solid interfaces.

Frequency-modulated charge transfer and ionic regulation in multi-interface dynamic EDLs

To systematically reveal the frequency dependence of charge transfer behavior at the liquid–solid interface, the EDL response was evaluated under different wave excitation frequencies. These measurements were performed under controlled laboratory tank conditions to identify the effective device-level excitation condition at the present experimental scale. As shown in Fig. 2a and Supplementary Fig. 27, the Q_{tr} and the I_{sc} both reached their peak values at an excitation

frequency of 0.7 Hz. At a frequency of 0.6 Hz, the low-frequency wave lacks sufficient energy to drive the gate liquid into contact with the drain electrode. As a result, the liquid–solid interface is only partially activated, and the device operates effectively in a single-electrode mode, thereby limiting charge transfer (Supplementary Fig. 28). In contrast, at higher frequencies such as 0.8 Hz, the rapid oscillation disrupted stable contact at the interface, and instances of liquid column retraction or breakage were frequently observed. Under such conditions, the liquid could not remain steadily in contact with the FEP surface, hindering the formation of a stable EDL. As a result, the interfacial charge distribution became sparse, and the effective response area decreased, leading to a substantial reduction in charge transfer efficiency, as shown in Supplementary Fig. 29a. The superior performance observed at 0.7 Hz is attributed to the most complete and sustained interaction between the liquid and the solid interface (Supplementary Fig. 29b). This condition allowed for optimal liquid–solid coupling and full development of the EDL, thereby enabling maximum power generation and interfacial regulation under the present controlled conditions.

The effect of liquid-phase composition on charge transfer performance was further examined. Using NaCl as a model electrolyte under controlled laboratory conditions, these measurements were designed to resolve the intrinsic concentration dependence of the dynamic EDL response and identify the mechanistic optimum of the present system. Specifically, both the Q_{tr} and the I_{sc} initially increased with rising Na^+ and Cl^- concentrations, reached a peak, and then declined. Optimal performance was achieved at an ion concentration of 10^{-4} mol L^{-1}, corresponding to a Q_{tr} of 0.8μC and an I_{sc} of 208.4 μA, as shown in Fig. 2b and Supplementary Fig. 30. This concentration-dependent behavior is attributed to two primary mechanisms. First, the restructuring of the EDL plays a critical role. At low ion concentrations, the limited availability of charge carriers impedes the formation of a compact inner Helmholtz plane (IHP), thereby constraining interfacial charge transfer (Fig. 2c). In contrast, at moderate concentrations such as 10^{-4} mol L^{-1}, enhanced ionic density promotes the formation of a denser and more stable IHP, which facilitates improved charge transduction (Fig. 2d). Second, changes in bulk solution conductivity further contribute to the observed trend. As ion concentration increases, the ohmic resistance of the electrolyte decreases, reducing energy loss during charge transport[40,41]. However, at excessively high concentrations, strong electrostatic screening effects become dominant. Specifically, When the solution detaches from the FEP surface, Na^+ cations adsorb at the interface, locally screening the negative charges on the FEP surface and thereby creating a pronounced interfacial screen effect that suppresses further electron transfer from interfacial water molecules, thus leading to deterioration of the EDL functionality[40,42,43](Fig. 2e and Supplementary Fig. 31). A similar concentration-dependent trend was also observed for $MgCl_2$ and $AlCl_3$ over the same concentration range (Supplementary Figs. 32 and 33), with the maximum response occurring at 10^{-4} mol L^{-1} in both cases. Accordingly, 10^{-4} mol/L is taken here as the optimal concentration for controlled mechanistic characterization of the present system. At the fixed cation concentration of 10^{-4} mol L^{-1}, replacing NaCl with $MgCl_2$ significantly enhanced the response, whereas $AlCl_3$ produced a markedly lower response (Fig. 2f and Supplementary Fig. 34). These results indicate that ion-specific effects cannot be interpreted simply as a monotonic dependence on valence. The enhancement observed for Mg^{2+} is attributed to its stronger electrostatic interaction, which may favor more compact interfacial adsorption and facilitate interfacial charge transfer. In contrast, although Al^{3+} has a higher nominal valence, it readily undergoes hydrolysis in aqueous media, generating $Al(OH)_3$ and releasing H^+, which enhances the screening or partial neutralization of the negatively charged FEP surface and thereby weakens the overall interfacial response[39]. Taken together, the distinct responses of different ions demonstrate that dynamic multi-interface EDLs can be selectively regulated through differences in valence and solvation/hydrolysis-related interfacial behavior. In the present study, Na^+ serves as the representative ion in the subsequent hydrospheric demonstrations, while the comparison with Mg^{2+} illustrates the ion-specific tunability of dynamic EDL responses. Beyond serving as charge carriers, ions possess discrete valence states and molecular identities, enabling them to convey not only electrical charge but also encoded information. This duality endows ion-based systems with unique capabilities distinct from conventional electronics. In living organisms, distinct ionic species encode and transmit physiological information through specialized pathways: Na^+ orchestrates osmotic balance and action potential dynamics, and Mg^{2+}, as an enzymatic cofactor, underpins energy metabolism and neuromuscular conduction[19,44,45]. Analogously, in iontronic systems, different ionic species act as discrete information carriers. Using Na^+ and Mg^{2+} as representative biologically relevant examples, even identical concentrations of these ions yield distinct dynamic responses and functionalities. Such ion-specific modulation of charge migration, selective gating, and local field interactions within confined interfaces enables the encoding of multiplexed information through variations in valence, hydration, and mobility. This capability establishes a bioinspired framework for low-power, adaptive coupling of energy and information (Fig. 2g). By harnessing these intrinsic ionic characteristics, iontronic architectures afford dynamic and reversible control of interfacial processes under minimal energy input, rendering them inherently compatible with aqueous and biological environments. Consequently, iontronics provides a versatile platform for energy-efficient information processing, adaptive sensing, and bioinspired energy-information flow that transcends the limitations of traditional semiconductor electronics.

Geometry-optimized multi-interface EDLs enable bioinspired, scalable energy flow

Three acrylic through-tubes with square, equilateral triangular, and circular cross-sections were fabricated, each maintaining the same effective solid-liquid contact area (Supplementary Fig. 35). Under identical wave-induced excitation, the fluid impact on both the outer interface and the drain region was comparable across all three geometries (Supplementary Fig. 36). Only minor variations in transferred charge were observed among the different geometries, indicating that the outer contour exerts minimal influence on charge transfer, as shown in Supplementary Fig. 37. The influence of source electrode geometry on charge transfer in dynamic multi-interface EDLs was evaluated using three configurations, each with an identical total copper area of 15.7 cm^2: a continuous wrapping structure (CW), a narrow-pitch periodic helix (NP), and a wide-pitch periodic helix (WP), as illustrated in Fig. 3a. In the CW configuration, a 5 cm-wide copper foil was tightly wrapped around the acrylic tube with zero pitch, forming a continuous conductive layer. The NP configuration employed a 2.5 cm-wide copper foil helically wrapped with a 1.0 cm pitch, generating periodic banded coverage with gaps. In the WP configuration, the same 2.5 cm foil was wrapped with a 3.5 cm pitch, producing a sparsely distributed electrode with wide intervals. As shown in Fig. 3b, the CW structure achieved the highest transferred charge (Q_{tr} = 0.8 μC), substantially exceeding NP (0.57 μC) and WP (0.47 μC), with the corresponding I_{sc} following the same trend (Supplementary Fig. 38). This pronounced difference is primarily attributed to the variation in effective interfacial area available for EDL activation, which is directly determined by the electrode geometry. To quantitatively describe this relationship, a geometric coverage factor (φ) was introduced:

$$\varphi = \frac{w}{w + p} \tag{3}$$

https://doi.org/10.1038/s41467-026-77636-4

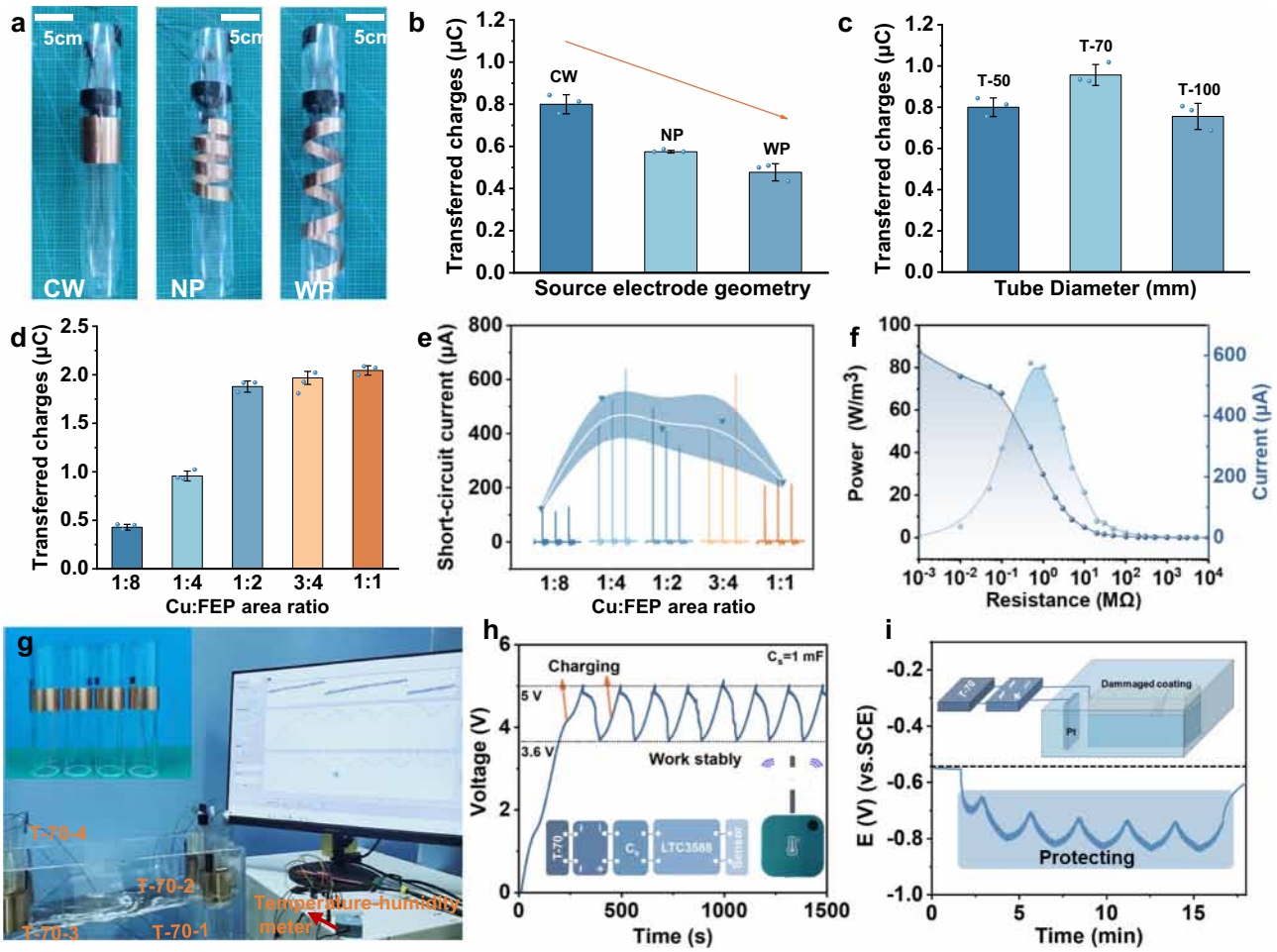


Fig. 3 | Scalable energy flow from a single device to an array in geometry-optimized multi-interface dynamic EDLs. a Photographs of three source-electrode geometries with the same total Cu area (15.7 cm^2): continuous wrapping (CW), narrow-pitch periodic helix (NP) and wide-pitch periodic helix (WP). **b** Transferred charge (Q_{tr}) for CW, NP, and WP source-electrode geometries. The arrow indicates the decrease in Q_{tr} with reduced source-electrode continuity. **c** Transferred charge (Q_{tr}) of acrylic through-tubes with different diameters (T-50, T-70, and T-100) under identical excitation. **d** Transferred charge (Q_{tr}) for different Cu:FEP area ratios (1:8, 1:4, 1:2, 3:4, 1:1) based on T-70. **e** Short-circuit current (I_{sc}) for different Cu:FEP area ratios (1:8, 1:4, 1:2, 3:4, 1:1) based on T-70. Three repeated wave-induced responses are shown for each ratio, with blue inverted triangles marking the mean peak I_{sc}. The white B-spline line guides the eye, and the shaded region denotes mean ± s.d. **f** Power density and Short-circuit current (I_{sc}) as functions of external load resistance. Symbols represent experimental data, and solid lines are guides to the eye connecting the data points. **g** Optical photograph of a prototype in which four T-70 multi-interface dynamic EDLs power a temperature-humidity sensor for real-time monitoring. **h** Charging of a 1 mF storage capacitor (C_s) by four devices and regulated output through an LTC3588 to 3.6 V, driving the temperature-humidity meter in stable operation. **i** Self-powered cathodic protection schematic diagram and potential variation curve of protected metal. In **b**, **c**, **d**, bars show mean values, dots indicate individual measurements, and error bars represent s.d. from three parallel measurements ($n = 3$). In **e**, the shaded region denotes s.d. from three repeated measurements.

where w is the width of each copper strip and p is the helical pitch. For the three configurations, the corresponding values are $\varphi_{CW} = 1.0$, $\varphi_{NP} = 0.714$, and $\varphi_{WP} = 0.417$. This indicates that the CW configuration achieves full interfacial activation (100%), while the NP and WP configurations retain only 71.4 and 41.7% of the effective area, respectively, due to their segmented layouts. The sequence of transferred charge (CW > NP > WP) closely follows the descending trend in geometric coverage, confirming a strong positive correlation between electrode continuity and charge transfer efficiency. More continuous electrode coverage leads to a larger dynamically activated EDLs area, thereby enhancing interfacial charge coupling and boosting overall output performance.

In addition, the Q_{tr} and I_{sc} performance of acrylic through-tube structures with different diameters (50, 70, and 100 mm) was evaluated under identical excitation conditions (T-50, T-70, and T-100). Among them, the T-70 exhibited the best performance, as shown in Fig. 3c and Supplementary Fig. 39. This optimal behavior can be interpreted as the result of a trade-off between geometric gain and excitation damping. As the tube diameter D increases, the effective interfacial area covered by the source electrode and FEP membrane increases approximately linearly with D, following $S_{EDL}(D) \propto \pi DH$, where H is the vertical height of the wetted region. When D increased from 50 mm to 70 mm, the linear gain in interfacial area dominated, leading to a significant enhancement in both Q_{tr} and I_{sc}. However, when D was further increased to 100 mm, the larger diameter induced stronger fluid resistance under wave excitation (Supplementary Fig. 40), reducing the displacement amplitude of the liquid column and compromising the interface contact integrity (Supplementary Fig. 41 and Supplementary Movie 2). As a result, despite the continued increase in area, the overall excitation was weakened, causing Q_{tr} and I_{sc} to decrease. After optimization of the diameter to 70 mm, the effect of the Cu:FEP area ratio on dynamic EDLs output was evaluated. With increasing copper area, a monotonic rise in Q_{tr} was observed, whereas the I_{sc} showed a pronounced non-monotonic dependence with a maximum at Cu: FEP = 1:4 (Fig. 3d, e). This peak is attributed to charge crowding at the liquid–solid interface near the drain. When the Cu area

increases, the active region for carrier collection and transfer expands, and the electrostatic repulsion at the negatively charged surface also strengthens. The competition between these effects yields an optimal area ratio for the I_{sc}, which is consistent with established models[46].

Under the optimized condition (0.7 Hz, 0.5 MΩ load), a peak power density of 82.2 W/m^3 per Hz was achieved (Fig. 3f), calculated using a core volume of 7.693×10^{-4} m^3. Remarkably, this performance surpasses previously reported comparable systems (Supplementary Fig. 42), highlighting its superior capability for power generation. Functionally, one device completes a closed route for collecting, storing and delivering energy from environmental input to the load, which is analogous to EODs generation and use in an individual weakly electric fish. A 2.2 μF capacitor was charged to 24 V in 60 s, and stable operation was maintained across 6.8–1000 μF (Supplementary Fig. 43). A warning lamp was powered directly by a single device (Supplementary Fig. 44 and Supplementary Movie 3). With multiple devices in parallel, power addition and regulated output were obtained, consistent with energy pooling in fish schools. Four devices in parallel pre-charged a 1 mF storage capacitor (C_s) for about 5 min. After regulation by an LTC3588 module, a stable 3.6 V output powered a temperature-humidity sensor and enabled continuous self-powered monitoring (Fig. 3g, h, Supplementary Figs. 45 and 46, and Supplementary Movie 4). The regulated output was further extended to self-powered cathodic protection in hydrospheric environments. During operation of the dynamic EDL system, the open-circuit potential of the protected metal (damaged coating sample) exhibited a pronounced and sustained negative shift, stabilizing within the corrosion protection window (Fig. 3i). This sustained cathodic polarization indicates that the metal potential is driven below its corrosion potential, thereby effectively suppressing anodic dissolution and corrosion processes. Mechanistically, the dynamically evolving EDL system delivers a continuous ionic-electronic coupled cathodic current to the metal surface, enabling corrosion protection without the need for external power input or sacrificial anodes. This establishes a self-powered protection mode driven directly by ambient mechanical energy harvesting. Furthermore, the results demonstrate a scalable architecture for functional deployment: a single device is sufficient for transient signal output and low-power applications, whereas parallelized arrays provide stable and continuous output suitable for long-term monitoring and self-powered corrosion protection. Collectively, these findings highlight the potential of the system as a multifunctional, self-sustained platform for energy harvesting and corrosion mitigation in aquatic environments.

Bioinspired hydrospheric sensing via information-encoded dynamic EDLs

At the hydrospheric interface, deploying intelligent systems requires not only energy conversion but also the real-time sensing of environmental information and spatial features. While the preceding sections establish multi-interface EDLs as an efficient self-powered unit, a further question is whether such local responses can be organized into a system capable of spatially resolved sensing. Weakly electric fish exemplify a mature biological strategy: their electroreceptors detect heterogeneous targets, including conductors and insulators that perturb the self-generated electric field. Signal encoding relies on the signed amplitude of the transepithelial potential, ΔV (Fig. 4a and Supplementary Fig. 47). The sign indicates whether local current lines converge or diverge, conveying directional and material information, while the magnitude scales with target distance, size, and conductivity contrast with water. Signals sampled in parallel by skin receptors propagate along neural pathways and are integrated within the electrosensory lateral line lobe, where local field disturbances are converted into spatiotemporal contrast codes. These codes encode both the identity and position of targets, enabling centimeter-scale electrolocation with high sensitivity. This contrast-based strategy provides a useful analog for the present system, in which local electrical responses must likewise be converted into spatially meaningful information.

Dynamic EDLs at liquid–solid interfaces provide an engineered analog to biological electrosensing. Wave-induced redistribution of charges within the EDL acts simultaneously as an energy source and an information carrier, mapped onto a bioinspired chain $\Delta S \rightarrow U \rightarrow I_{sc}$, where $\Delta S = S_t - S_0$ represents the change in effective responsive area on FEP (the spatially dependent perturbation), U reflects the interfacial potential modulation, and I_{sc} corresponds to the measured short-circuit current. As expressed in Eq. (1), the sign of ΔS determines current polarity, while its magnitude sets current strength. Accordingly, polarity and amplitude of the EDL response together establish a contrast-like encoding rule, through which local perturbations can be translated into interpretable electrical signatures. By adjusting the drain position relative to the interface, the polarity of ΔS and thus I_{sc}, can be controlled: near-end drains yield $S_t > S_0$ and positive currents (Supplementary Fig. 48), whereas far-end drains produce $S_t < S_0$ and negative currents (Supplementary Fig. 49). Under near-end conditions ($\Delta S > 0$), wave motion maintains $S_t > S_0$ throughout the cycle, rendering I_{sc} consistently positive; the relative amplitude of I_{sc} thereby encodes environmental information, analogous to contrast coding in weakly electric fish, where relative differences rather than absolute potentials convey sensory cues. This principle enables in situ coating inspection and early warning: an intact insulating coating maintains an open circuit with dormant EDLs and near-zero I_{sc}. Local damage exposes a conductive substrate, establishing an ion-electron coupled dynamic EDL and generating a strong positive warning current under wave excitation (Supplementary Figs. 50 and 51 and Supplementary Movie 5). Furthermore, the same framework allows real-time grading of wave conditions: small waves produce low-amplitude pulses (~100–200 μA), medium waves yield higher-density pulses (~300–400 μA), and large waves reach peak amplitudes with symmetric decay as waves subside (Supplementary Fig. 52 and Supplementary Movie 6). The relative I_{sc} magnitude thus functions as a robust physical marker for environmental monitoring and warning.

Moreover, as described above, the sign of ΔS can be modulated by the relative position of the drain to the interface, revealing the liquid–solid interface's intrinsic spatial selectivity and nonlinear sensitivity to external perturbations. This feature underpins the development of a spatially resolvable sensing system. Inspired by group electrolocation in weakly electric fish, a main-auxiliary (M@A) network was constructed for two-dimensional cooperative sensing. The main drain (M) at the near end captured strong local signals, analogous to the focal sensing of the fish itself, while auxiliary (A) drains were positioned in four regions, northwest (NW), southwest (SW), northeast (NE), and southeast (SE), to detect distributed disturbances and cooperate with the main drain, analogous to conspecific contributions (Fig. 4b, c). This architecture was not introduced simply to increase the number of sensing nodes. Instead, it organizes local EDL responses from different positions into a coordinated spatial pattern that can be jointly decoded, rather than treating them as isolated local outputs. In this sense, the M@A network provides an engineered analog to the collective electrolocation strategy of weakly electric fish. Multi-point acquisition and cooperative analysis were implemented via a LabVIEW platform. Dynamic electrode coupling was mapped to two-dimensional spatial patterns, enabling directional gain and spatial decoding (Fig. 4d and Supplementary Movie 7). A one-to-one correspondence was observed between the polarity and magnitude of auxiliary I_{sc} and spatial location (Fig. 4e): near-end NW and SW regions exhibited positive currents (slightly lower in SW), while far-end NE and SE regions were negative (SE weakest). Under M@A cooperation, near-end signals added constructively, far-end signals formed a clear bidirectional composite pattern (Supplementary Figs. 53–56), and cumulative charge transfer exceeded individual contributions from M or A. For instance, in the NW region, M@A achieved 2.0 μC, surpassing

https://doi.org/10.1038/s41467-026-77636-4

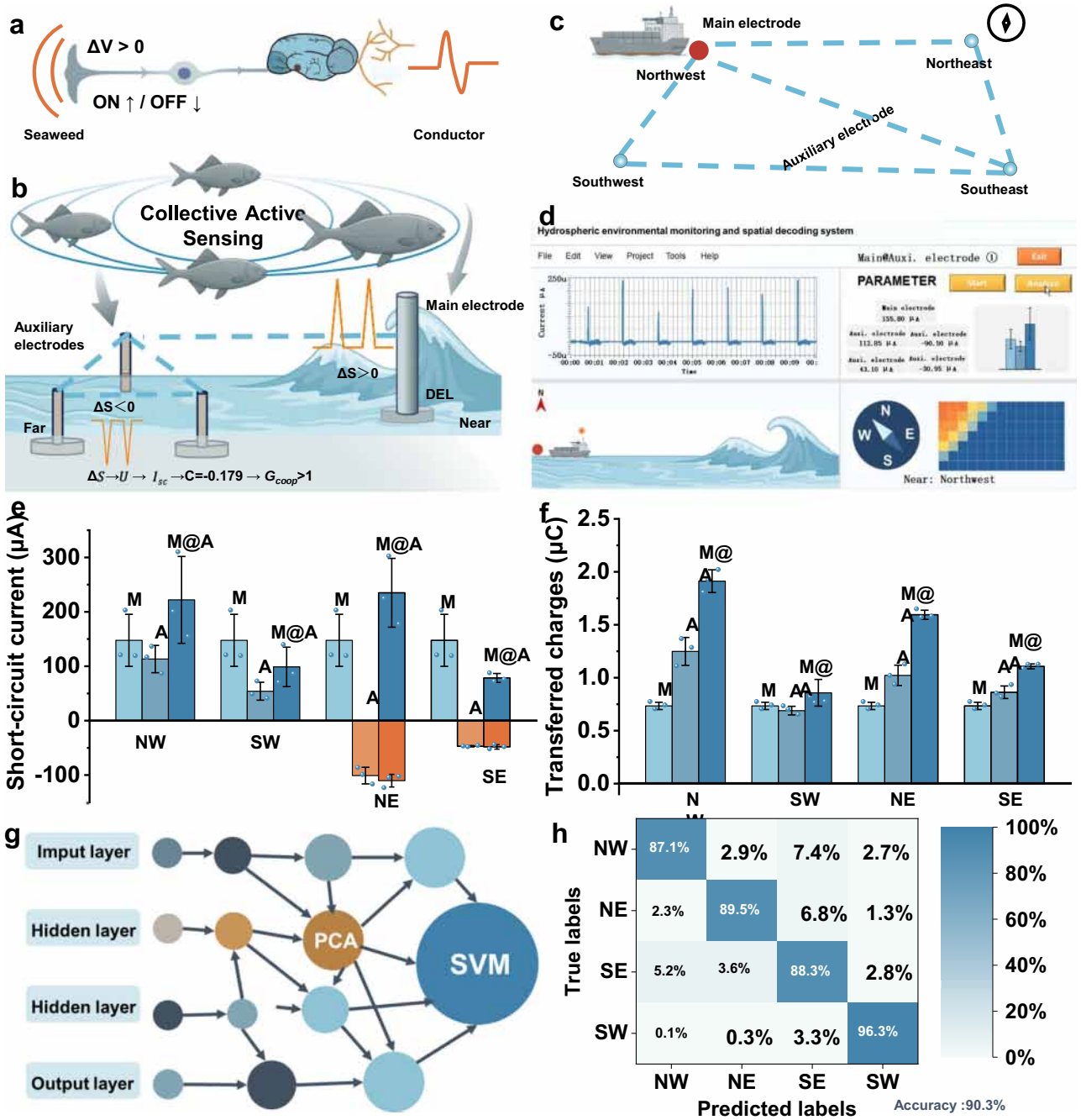


Fig. 4 | Bio-inspired spatial sensing via main-auxiliary electrode cooperation. **a** Schematic diagram of a weakly electric fish perceiving the spatial position of a conductor target through spatiotemporal contrast coding. Object-induced field perturbations generate a signed potential contrast (ΔV), producing enhanced or reduced electrosensory responses. **b** Concept of collective active sensing and its electrical double layers (EDLs) analog. Auxiliary electrodes at far positions and a main electrode at the near position convert wave-induced changes in effective responsive area (ΔS) into interfacial potential modulation (U) and short-circuit current (I_{sc}), enabling spatial contrast (C) and cooperative gain (G_{coop}). The arrows indicate cooperative signal transfer and the ΔS-U-I_{sc}-C-G_{coop} conversion pathway. **c** Two-dimensional deployment of the main electrode and auxiliary electrodes for cooperative sensing in the northwest (NW), southwest (SW), northeast (NE) and southeast (SE) regions. **d** LabVIEW-based platform for synchronous data acquisition and real-time direction discrimination. **e** Short-circuit current (I_{sc}) in each region for the main electrode alone (M), auxiliary electrode alone (A) and main-auxiliary cooperative mode (M@A). **f** Transferred charge (Q_{tr}) in each region for the M, A and M@A modes. **g** Principal component analysis-support vector machine (PCA-SVM) classification workflow. **h** Normalized confusion matrix of spatial-recognition results, showing an overall accuracy of 90.3%. In **e** and **f**, bars show mean values, dots indicate individual measurements and error bars represent s.d. from three parallel measurements ($n = 3$).

0.7 μC for M and 1.25 μC for A, while even the weak SE region exhibited measurable signal gain (Fig. 4f).

For quantitative evaluation, two dimensionless metrics were introduced. First, the spatial contrast C, defined by a normalized difference between near and far amplitudes, measures spatial separation and discriminability. A larger absolute value of C indicates stronger near-far contrast. The calculated values were $C_M = 0.000$, $C_A = 0.062$, and $C_{M@A} = -0.179$ (Supplementary Note 3). Under M sensing, the near and far means were both 147.6 μA and the contrast was zero, so no spatial difference was present. Under A sensing, a slight near-end

advantage appeared with a near mean of 83.7 μA and a far mean of 73.95 μA, which gave C = 0.062. Under the cooperative mode M@A, the near mean was 160.4 μA and the far mean increased to 230.8 μA, which gave C = −0.179. This shows that cooperation favors the far end rather than a simple near-end add-up. The effect enhances local differences and suppresses common-mode background, consistent with contrast coding in weakly electric fish. The second was the cooperative gain (G_{coop}), defined as (Supplementary Note 4):

$$G_{coop} = \frac{Q_{tr}(M@A)}{\max\{Q_{tr}(M), Q_{tr}(A)\}} \quad (4)$$

All gains were above 1, namely 1.532 in the northwest region, 1.169 in the southwest region, 1.561 in the northeast region, and 1.283 in the southeast region, with an average of 1.386. The far-end average gain was higher, with G_{far} = 1.422 and G_{near} = 1.351. Thus, cooperation not only increases overall output but also preferentially improves far-end sensing, in agreement with cooperative enhancement among conspecific EODs in group electrolocation. Main-auxiliary cooperation, therefore, integrated polarity and amplitude, boosted output, and enhanced spatial contrast. To achieve efficient recognition of multi-class signals, the raw M@A cooperative sensing data were directly employed as input features and subjected to principal component analysis (PCA) for dimensionality reduction. PCA minimized multicollinearity among variables and suppressed noise interference, thereby isolating the most representative signal features. The dimension-reduced data were subsequently classified using a support vector machine (SVM) with a radial basis function (RBF) kernel to enhance nonlinear separability (Fig. 4g). The dataset was divided into training and testing subsets in a 70/30% ratio, and classification performance was assessed using a normalized confusion matrix. The results reveal that this strategy effectively captures the temporal dynamics of the signals, achieving an overall recognition accuracy of 90.3% (Fig. 4h). Directional enhancement and spatial decoupling were realized, establishing a self-powered and adaptive framework for spatial target recognition and ship localization, with promising implications for autonomous sensing and navigation applications.

To further assess the scalability of the M@A localization strategy, localization experiments were conducted in a larger-scale tank configuration, where the effective separation between the main and auxiliary drains was increased. Despite the longer propagation path and more complex signal-transmission conditions, the M@A network still maintained spatially resolvable responses and enabled reliable discrimination of target position (Supplementary Fig. 57). Quantitative analysis further supports this result: M@A operation yielded a markedly enhanced spatial contrast (C = − 0.292) and cooperative gain values consistently above unity (mean G_{coop} = 1.469), confirming effective cooperative localization at the larger scale. Detailed regional data are provided in Supplementary Tables S3 and Supplementary Tables S4.

Discussion

This work establishes a dynamic multi-interface EDLs platform that unifies power generation and information transmission within a single physical architecture. By coupling an outer FEP-water interface with an inner PMMA-water interface in an acrylic through-tube, wave-induced disturbances periodically assemble and disassemble interfacial EDLs, initiating charge-relay and parallel-release processes that significantly enhance Q_{tr} and I_{sc}, nearly doubling performance compared with single-interface systems. This synchronized interfacial activation enables efficient energy conversion, producing outputs sufficient to drive warning lights, low-power sensors, and self-powered corrosion protection, highlighting the practical potential of the platform for hydrospheric applications. Beyond energy capture, the dynamic redistribution of interfacial ionic carriers functions as a decodable information carrier. Drawing inspiration from the contrast-coding strategy of weakly electric fish, the sign and magnitude of the EDL response are mapped into spatially interpretable electrical signatures, enabling predictive coating monitoring and real-time wave-state recognition. Extending this concept, a main-auxiliary drain network inspired by cooperative sensing in fish schools establishes a bioinspired electrosensory system for directional signal amplification and two-dimensional spatial decoding at open hydrospheric interfaces. In this way, the present platform moves beyond previous EDL studies centered on localized interfacial manipulation by enabling cooperative operation of dynamic multi-interface EDLs in open hydrospheric environments. It therefore extends EDL-based self-powered sensing from localized unit-level response to distributed spatial sensing in aquatic environments. Although demonstrated in controlled laboratory water domains, this work establishes an exploratory proof-of-concept for scalable self-powered sensing in realistic aquatic environments. The low-cost, tubular architecture is compatible with distributed deployment, while practical translation will require validation under more realistic hydrodynamic conditions and improved long-term robustness.

Methods

Materials and reagents

Acrylic tubes, 30-μm-thick fluorinated ethylene propylene (FEP) film and FEP rods were purchased from Alibaba. Sodium chloride (NaCl, ≥99%), magnesium chloride ($MgCl_2$, ≥99%) and aluminum chloride ($AlCl_3$, ≥99%) were purchased from Aladdin. The DI water with a resistivity of 18.2 MΩ·cm used here was produced by a deionizer (HHitech, China). Unless otherwise stated, all chemical reagents were of analytical grade and used without further treatment.

Fabrication of single- and multi-interface EDL devices

The SI-BT was fabricated using an acrylic blind tube with an outer diameter of 50 mm, a wall thickness of 3 mm and a height of 30 mm. Copper foil was attached to the outer wall of the acrylic tube as the source electrode, and a lead wire was connected to the copper foil. A FEP film with a thickness of 30 micrometers and a width of 200 mm was then laminated onto the outer wall to fully cover the copper foil and form the outer dielectric-water interface. A copper wire with a diameter of 0.3 mm was used as the drain electrode.

Control devices were prepared to distinguish single-interface operation, geometrical interfacial multiplication and true multi-interface coupling. The SI-BT-O was prepared by filling the blind tube with insulating oil. The pseudo-interface blind-tube systems were prepared by filling the blind tube with either deionized water (PI-BT-W) or NaCl solution (PI-BT-N), thereby producing geometrically dual but hydraulically isolated inner and outer interfaces. The SI-FR was prepared by replacing the acrylic blind tube with a solid FEP rod while keeping the remaining electrode configuration unchanged.

The MI-ST was prepared by replacing the blind tube with an acrylic through-tube, which connected the inner and outer liquid pathways and allowed coupled activation of the inner and outer solid-liquid interfaces. The CI-IS was derived from the through-tube geometry by sealing the upper port so that the inner-wall liquid remained quiescent under mechanical excitation. The MI-PT was formed by adding an additional drain electrode along the inner wall of the MI-ST device and electrically connecting the inner and outer drain electrodes, enabling synchronized charge release from coupled interfaces. The EA-SI was fabricated by replacing the tubular acrylic substrate with a flat acrylic plate while preserving the same copper foil/FEP electrode configuration and effective single-interface area as in the MI-ST device.

Preparation of coated steel specimens

Coated steel specimens were prepared according to ISO 12944. For coating-monitoring and early-warning measurements, intact coated specimens were used as the reference state. To establish an electrical connection for signal recording, one corner of the coating was gently polished with sandpaper to expose the underlying steel substrate, and the lead wire was routed to the electrometer for current measurement. Artificial coating damage was produced by mechanically removing a defined area of the coating until the steel substrate was exposed, thereby simulating coating breakdown. Damaged coated specimens used for self-powered cathodic-protection measurements were prepared using the same coating-removal procedure, and the exposed metal region served as the protected/working area. The exposed damage area is indicated in Supplementary Fig. 51.

PCA-SVM classification for spatial recognition

To preserve the integrity of experimentally acquired main-auxiliary (M@A) cooperative sensing signals, invalid or missing points in the current time-series data were filled by linear interpolation. This preprocessing retained the temporal variation of the measured EDLs responses and generated complete, standardized 25-dimensional feature vectors for each sample. PCA was then applied to the high-dimensional feature vectors to reduce multicollinearity among redundant sensing parameters, suppress measurement noise through orthogonal feature transformation and extract the dominant components for classification. A supervised SVM with an RBF kernel was used for multi-class spatial recognition. The RBF kernel was selected to capture the nonlinear mapping relationship in the cooperative current-response features and to enhance separability among different spatial categories by maximizing the classification margin. The dataset was randomly divided into a training set (70%) and an independent testing set (30%), and the classification performance was evaluated using a normalized confusion matrix.

Numerical simulations of wave-induced liquid motion

Ansys Fluent was used to simulate the wave-induced liquid motion that drives dynamic electrical double layer formation at solid-liquid interfaces. A three-dimensional transient air-water two-phase CFD model based on the volume of fluid (VOF) method was employed to track the free-surface motion and hydrodynamic perturbation around the cylindrical device structure. Detailed settings and calculations are provided in Supplementary Note 5.

Self-powered cathodic-protection measurements

Self-powered cathodic protection was evaluated in a conventional three-electrode system, where platinum foil, a saturated calomel electrode (SCE), and the damaged coated specimen served as the counter (CE), reference (RE), and working (WE) electrodes, respectively. The electrolyte was a 3.5 wt% NaCl solution, and the open-circuit potential was recorded using an electrochemical workstation (CHI760E, Shanghai Chen Hua, China).

Characterization and measurements

Wave excitation was provided by a six-degree-of-freedom motion platform (NJLJ-6D(R)-60, Lingjing Technology, China). Unless otherwise specified, the platform was operated in a horizontal reciprocating mode at 0.7 Hz with a stroke of 62 mm. Strokes of 50, 56 and 62 mm were used to emulate small, medium and large waves, respectively. The programmable motion platform provided repeatable kinematic inputs, ensuring consistent mechanical forcing conditions across different excitation frequencies (Supplementary Fig. 58).

Unless otherwise stated, measurements were performed in a water tank with dimensions of 500 × 200 × 300 mm and a water depth of 150 mm. For larger-scale localization experiments, a larger tank with dimensions of 1500 × 200 × 300 mm and a water depth of 100 mm was used to increase the effective separation between the main and auxiliary drains. In this configuration, the platform was operated at 0.3 Hz with a stroke of 80 mm to maintain stable wave propagation for spatial localization measurements.

Electrical output signals were recorded using an electrometer and a data-acquisition unit (6514, Keithley; BNC-2120, National Instruments). Static contact angles were measured using a contact angle system (OCA-20, DataPhysics Instruments, Germany).

Data availability

The data supporting the findings of this study are reported in the main text or the Supplementary Information. All raw experimental data relevant to this study are available from the corresponding author upon request. Source data are provided with this paper.

References

1. Ratnarajah, L. et al. Monitoring and modelling marine zooplankton in a changing climate. *Nat. Commun.* **14**, 564 https://doi.org/10.1038/s41467-023-36241-5 (2023).
2. Kroodsma, D. A. et al. Tracking the global footprint of fisheries. *Science* **359**, 904–908 https://doi.org/10.1126/science.aao5646 (2018).
3. Roberts, J. M. et al. A blueprint for integrating scientific approaches and international communities to assess basin-wide ocean ecosystem status. *Commun. Earth Environ.* **4**, 12 https://doi.org/10.1038/s43247-022-00645-w (2023).
4. Paolo, F. S. et al. Satellite mapping reveals extensive industrial activity at sea. *Nature* **625**, 85–91 https://doi.org/10.1038/s41586-023-06825-8 (2024).
5. Gao, S., Peng, Z., Wang, H., Liu, L. & Wang, D. Safety-critical model-free control for multi-target tracking of USVs with collision avoidance. *IEEE/CAA J. Automat. Sin.* **9**, 1323–1326 https://doi.org/10.1109/jas.2022.105707 (2022).
6. Piazzolla, D. et al. Combining USV ROV and multimetric indices to assess benthic habitat quality in coastal areas. *Sci. Rep.* **15**, 24282 https://doi.org/10.1038/s41598-025-09845-8 (2025).
7. Xing, F. et al. High-entropy energy for self-powered systems. *SmartSys* **1**, e70001 https://doi.org/10.1002/sys3.70001 (2025).
8. Saeed, N., Celik, A., Al-Naffouri, T. Y. & Alouini, M.-S. Underwater optical wireless communications, networking, and localization: a survey. *Ad Hoc Netw.* **94**, 101935 https://doi.org/10.1016/j.adhoc.2019.101935 (2019).
9. Li, Z., Chitre, M. & Stojanovic, M. Underwater acoustic communications. *Nat. Rev. Electr. Eng.* **2**, 83–95 https://doi.org/10.1038/s44287-024-00122-w (2025).
10. Quaade, S., Vallebueno, A., Alcabes, O. D. N., Rodolfa, K. T. & Ho, D. E. Remote sensing and computer vision for marine aquaculture. *Sci. Adv.* **10**, eadn4944 https://doi.org/10.1126/sciadv.adn4944 (2024).
11. Rutter, J. D. et al. Immersion patterns alone can predict vessel following by albatrosses. *J. Appl. Ecol.* **62**, 1831–1843 https://doi.org/10.1111/1365-2664.70085 (2025).
12. Wu, J. Understanding the electric double-layer structure, capacitance, and charging dynamics. *Chem. Rev.* **122**, 10821–10859 https://doi.org/10.1021/acs.chemrev.2c00097 (2022).
13. Schott, C. M. et al. How to assess and predict electrical double layer properties. implications for electrocatalysis. *Chem. Rev.* **124**, 12391–12462 https://doi.org/10.1021/acs.chemrev.3c00806 (2024).
14. Zhou, Y. et al. Real-time mass spectrometric characterization of the solid-electrolyte interphase of a lithium-ion battery. *Nat. Nanotechnol.* **15**, 224–230 https://doi.org/10.1038/s41565-019-0618-4 (2020).
15. Li, Z. et al. High-frequency supercapacitors surpassing dynamic limit of electrical double layer effects. *Nat. Commun.* **16**, 3704 https://doi.org/10.1038/s41467-025-59015-7 (2025).

16. Wang, Z. L. & Wang, A. C. On the origin of contact-electrification. *Mater. Today* **30**, 34–51 https://doi.org/10.1016/j.mattod.2019.05.016 (2019).
17. Lin, S., Xu, L., Chi Wang, A. & Wang, Z. L. Quantifying electron-transfer in liquid-solid contact electrification and the formation of electric double-layer. *Nat. Commun.* **11**, 399 https://doi.org/10.1038/s41467-019-14278-9 (2020).
18. Chen, W. et al. Cascade-heterogated biphasic gel iontronics for electronic-to-multi-ionic signal transmission. *Science* **382**, 559–565 https://doi.org/10.1126/science.adg0059 (2023).
19. Qian, H., Wei, D. & Wang, Z. Bionic iontronics based on nano-confined structures. *Nano Res.* **16**, 11718–11730 https://doi.org/10.1007/s12274-023-5705-z (2023).
20. Long, Y., Zhao, B., Liu, M., Hu, W. & Pu, X. Smart hydrogel tactile sensors and systems: a comprehensive review. *SmartSys* **1**, e70015 https://doi.org/10.1002/sys3.70015 (2026).
21. Li, X., Amaratunga, G., Wang, Z. L. & Wei, D. Unlocking interfacial charge at dielectric solid–liquid interfaces via triboelectric nanogenerator probe. *SmartSys* **2**, e70019 https://doi.org/10.1002/sys3.70019 (2026).
22. Zhang, N., He, Y. & Wang, L. Designing iontronic pressure sensors: a perspective from multiscale mechanics. *Iontronics* **1**, 5 https://doi.org/10.20517/iontronics.2025.05 (2025).
23. Wang, X. et al. Flexible iontronic pressure sensing technology: advanced structural ionic layer. *Iontronics* https://doi.org/10.20517/iontronics.2026.01 (2026).
24. Li, X., Cheng, T., Wang, Z. L. & Wei, D. Neuromimetic circuits enabled by dynamic regulation of the electrical double layer. *npj Flex. Electron.* **9**, 66 https://doi.org/10.1038/s41528-025-00450-3 (2025).
25. Li, L. et al. Sparking potential over 1200 V by a falling water droplet. *Sci. Adv.* **9**, eadi2993 https://doi.org/10.1126/sciadv.adi2993 (2023).
26. Yin, J. et al. Waving potential in graphene. *Nat. Commun.* **5**, 3582 https://doi.org/10.1038/ncomms4582 (2014).
27. Li, J., Yin, J. & Guo, W. Hydrovoltaic energy and intelligence: where ions meet electrons. *Iontronics* **1**, 3 https://doi.org/10.20517/iontronics.2025.03 (2025).
28. Li, X., Wang, Z. L. & Wei, D. Scavenging energy and information through dynamically regulating the electrical double layer. *Adv. Funct. Mater.* **34**, 2405520 https://doi.org/10.1002/adfm.202405520 (2024).
29. Li, X., Li, R., Li, S., Wang, Z. L. & Wei, D. Triboiontronics with temporal control of electrical double layer formation. *Nat. Commun.* **15**, 6182 https://doi.org/10.1038/s41467-024-50518-3 (2024).
30. Li, X. et al. Harnessing triboiontronic Maxwell's demon by triboelectric-induced polarization for efficient energy-information flow. *Joule* **9**, 101888 https://doi.org/10.1016/j.joule.2025.101888 (2025).
31. Yang, F. et al. Vertical iontronic energy storage based on osmotic effects and electrode redox reactions. *Nat. Energy* **9**, 263–271 https://doi.org/10.1038/s41560-023-01431-4 (2024).
32. Zhang, J., Lin, S., Zheng, M. & Wang, Z. L. Triboelectric nanogenerator as a probe for measuring the charge transfer between liquid and solid surfaces. *ACS Nano* **15**, 14830–14837 https://doi.org/10.1021/acsnano.1c04903 (2021).
33. Lavoue, S. et al. Comparable ages for the independent origins of electrogenesis in African and South American weakly electric fishes. *PLoS ONE* **7**, e36287 https://doi.org/10.1371/journal.pone.0036287 (2012).
34. Pedraja, F. & Sawtell, N. B. Collective sensing in electric fish. *Nature* **628**, 139–144 https://doi.org/10.1038/s41586-024-07157-x (2024).
35. Catania, K. The shocking predatory strike of the electric eel. *Science* **346**, 1231–1234 https://doi.org/10.1126/science.1260807 (2014).
36. Gabbiani, F., Metzner, W., Wessel, R. & Koch, C. From stimulus encoding to feature extraction in weakly electric fish. *Nature* **384**, 564–567 https://doi.org/10.1038/384564a0 (1996).
37. Moller, P. Electric signals and schooling behavior in a weakly electric fish, *Marcusenius cyprinoides* L. (Mormyriformes). *Science* **193**, 697–699 https://doi.org/10.1126/science.948747 (1976).
38. Schwarz, S. & von der Emde, G. Distance discrimination during active electrolocation in the weakly electric fish *Gnathonemus petersii*. *J. Comp. Physiol. A* **186**, 1185–1197 https://doi.org/10.1007/s003590000170 (2000).
39. Zhang, H. et al. Fabrication of tubular electricity nanogenerator with high power density by bulk effect. *Adv. Funct. Mater.* https://doi.org/10.1002/adfm.202424446 (2025).
40. Nie, J. et al. Probing contact-electrification-induced electron and ion transfers at a liquid–solid interface. *Adv. Mater.* **32**, 1905696 https://doi.org/10.1002/adma.201905696 (2019).
41. Cai, C. et al. Advanced triboelectric materials for liquid energy harvesting and emerging application. *Mater. Today* **52**, 299–326 https://doi.org/10.1016/j.mattod.2021.10.034 (2022).
42. Zhang, H. et al. Liquid-based nanogenerator fabricated by a self-assembled fluoroalkyl monolayer with high charge density for energy harvesting. *Matter* **5**, 1466–1480 https://doi.org/10.1016/j.matt.2022.02.013 (2022).
43. Liu, J. et al. Nonaqueous contact-electro-chemistry via triboelectric charge. *J. Am. Chem. Soc.* **146**, 31574–31584 https://doi.org/10.1021/jacs.4c09318 (2024).
44. de Baaij, J. H. F., Hoenderop, J. G. J. & Bindels, R. J. M. Magnesium in man: implications for health and disease. *Physiol. Rev.* **95**, 1–46 https://doi.org/10.1152/physrev.00012.2014 (2015).
45. Lifton, R. P., Gharavi, A. G. & Geller, D. S. Molecular mechanisms of human hypertension. *Cell* **104**, 545–556 https://doi.org/10.1016/S0092-8674(01)00241-0 (2001).
46. Nan, Y. et al. Submerged and completely open solid–liquid triboelectric nanogenerator for water wave energy harvesting. *InfoMat* **7**, e12621 https://doi.org/10.1002/inf2.12621 (2025).

Author contributions

Y.N., X.L., X.W., B.C., D.W., and Z.L.W. proposed the concept and initiated the project. Y.N. carried out the experiments in this paper and analyzed the corresponding data. Y.N., X.L., X.W., and D.W. drafted and revised the manuscript. Y.D. designed and implemented the PCA-RBF-SVM-based machine learning classification method for multi-class signal recognition. J.H. performed numerical simulations of the mechanically induced dynamic EDL process using Ansys Fluent. R.H. completed the LabVIEW programming. All the authors discussed the results and commented on the manuscript.

Funding

This work was supported by the National Natural Science Foundation of China (No. 42476207), National Natural Science Foundation (No. 22479016), National Key Research and Development Program of China (No. 2023YFB2604600), the Key Research and Development Program of Shandong Province, China (No.2026CXPT224) , the Self-Hosting Project by the Institute of Oceanology (No. IOCASZZZX105), and the Flexible Talent Innovation Platform Project in Hainan Province (No. RXPTXM202610), Shandong Postdoctoral Science Foundation (No. SDBX2024045), China Postdoctoral Science Foundation (No. 2025M781041), and Postdoctoral Fellowship Program of China Postdoctoral Science Foundation (No. GZC20260537).

Competing interests

The authors declare no competing interests.

Additional information

Supplementary information The online version contains supplementary material available at https://doi.org/10.1038/s41467-026-77636-4.

Correspondence and requests for materials should be addressed to Xiutong Wang, Baodong Chen, Zhong Lin Wang or Di Wei.

Peer review information *Nature Communications* thanks Bin Luo, Daoai Wang, Bin Kang, and the other, anonymous, reviewer(s) for their contribution to the peer review of this work. A peer review file is available.

Reprints and permissions information is available at http://www.nature.com/reprints

Publisher's note Springer Nature remains neutral with regard to jurisdictional claims in published maps and institutional affiliations.

Open Access This article is licensed under a Creative Commons Attribution-NonCommercial-NoDerivatives 4.0 International License, which permits any non-commercial use, sharing, distribution and reproduction in any medium or format, as long as you give appropriate credit to the original author(s) and the source, provide a link to the Creative Commons licence, and indicate if you modified the licensed material. You do not have permission under this licence to share adapted material derived from this article or parts of it. The images or other third party material in this article are included in the article's Creative Commons licence, unless indicated otherwise in a credit line to the material. If material is not included in the article's Creative Commons licence and your intended use is not permitted by statutory regulation or exceeds the permitted use, you will need to obtain permission directly from the copyright holder. To view a copy of this licence, visit http://creativecommons.org/licenses/by-nc-nd/4.0/.

© The Author(s) 2026